

Coil–Helix Block Copolymers Can Exhibit Divergent Thermodynamics in the Disordered Phase

Michael J. Grant, Brennan J. Fingler, Natalie Buchanan, and Poornima Padmanabhan*



Cite This: <https://doi.org/10.1021/acs.jctc.3c00680>



Read Online

ACCESS |



Metrics & More

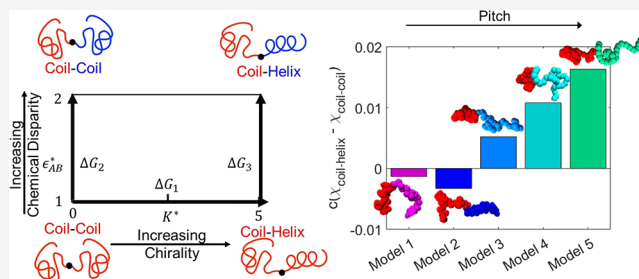


Article Recommendations



Supporting Information

ABSTRACT: Chiral building blocks have the ability to self-assemble and transfer chirality to larger hierarchical length scales, which can be leveraged for the development of novel nanomaterials. Chiral block copolymers, where one block is made completely chiral, are prime candidates for studying this phenomenon, but fundamental questions regarding the self-assembly are still unanswered. For one, experimental studies using different chemistries have shown unexplained diverging shifts in the order–disorder transition temperature. In this study, particle-based molecular simulations of chiral block copolymers in the disordered melt were performed to uncover the thermodynamic behavior of these systems. A wide range of helical models were selected, and several free energy calculations were performed. Specifically, we aimed to understand (1) the thermodynamic impact of changing the conformation of one block in chemically identical block copolymers and (2) the effect of the conformation on the Flory–Huggins interaction parameter, χ , when chemical disparity was introduced. We found that the effective block repulsion exhibits diverging behavior, depending on the specific conformational details of the helical block. Commonly used conformational metrics for flexible or stiff block copolymers do not capture the effective block repulsion because helical blocks are semiflexible and aspherical. Instead, pitch can quantitatively capture the effective block repulsion. Quite remarkably, the shift in χ for chemically dissimilar block copolymers can switch sign with small changes in the pitch of the helix.



INTRODUCTION

Chirality is a ubiquitous feature of nature that arises when an object's mirror image is not superimposable with itself. It plays a pivotal role in a variety of fields such as biology, drug discovery, structural color, and optics.^{1–5} For example, porphyrin assemblies are surrounded by helical proteins in chlorophyll that enhance their light capturing capabilities required for photosynthesis.⁶ Interestingly, even achiral porphyrins have spontaneously formed chiral supramolecular assemblies showing the possibility of producing completely chiral structures from achiral building blocks.^{7–9} From this biological inspiration, chirality transfer has been leveraged in engineering numerous synthetic functional materials such as those capable of circularly polarized luminescence,¹⁰ immune regulation,¹¹ chiral induced spin selectivity,¹² and asymmetric catalysis.¹³ Yet, even with an abundance of known examples, the transfer of chirality across multiple length scales is not completely understood.

The relationship between chirality and self-assembly via thermodynamics has been recently investigated through the use of block copolymers (BCPs).^{14–21} In typical BCPs, two chemically distinct polymers are connected end-to-end by a covalent bond. The repulsion between these two blocks drives phase separation, but the covalent linkage limits the length scale of assembly to the micro- or mesoscale. A wide variety of

morphologies can be obtained and the thermodynamics that drive their characteristic phase diagrams have been widely studied for flexible and semiflexible BCPs.^{22–27} Interestingly, when one block of a BCP is made completely chiral, the conformations of that block also become helical. Such a conformational change can significantly perturb the phase diagram—so much so that a novel, albeit metastable, helical phase emerged for chiral polystyrene-*b*-poly(L-lactic acid) (PS-*b*-PLLA).^{28,29} This phenomenal discovery introduced the concept that chirality can fundamentally alter the thermodynamics of BCP self-assembly and could lead to novel morphologies and applications. Following this, a theoretical description of chiral self-assembly (orientational self consistent field theory, oSCFT) expanded the phase diagram along a new dimension to account for twist-like interactions, confirming the presence of a thermodynamically stable helical phase.^{30–32} Subsequent experimental studies showed that poly(benzyl

Special Issue: Computational and Theoretical Studies Focused on Self-Assembly and Molecular Organization

Received: June 21, 2023



methacrylate)-*b*-poly(D-cyclohexylglycolide) (PBM–PDCG) self-assembled into a stable, helical phase.³³ The reason for the stability in this chemistry was postulated to come from the bulkier chiral side group of the PDCG when compared to PLLA, which would have enhanced the strength of the chiral interactions, an important parameter in oSCT. This suggested that the mere presence of chirality is not sufficiently descriptive to describe the changing phase behavior; rather, one must account for the strength of chirality.

The introduction of chirality-driven helical conformations affects the thermodynamics and impacts nonchiral phases as well, including the disordered phase. Ho et al. found that relative to the achiral PS-*b*-PLA, the chiral PS-*b*-PLLA led to an increase in the order–disorder transition temperature (T_{ODT}).²⁸ This shift was hypothesized to occur due to chirality enhancing the incompatibility between the PS and PLLA blocks. For a different model chiral BCP (poly(*n*-butyl acrylate)-*b*-polypeptoid, PnBA-*b*-polypeptoid), chirality was found to affect the domain sizes of the cylindrical (also achiral) morphology and T_{ODT} .²¹ To investigate the T_{ODT} more closely, Yu et al. examined the effect of chirality on both the disordered and lamellar phases.³⁴ Conformationally, they observed an increase in the persistence length and a decrease in the radius of gyration in the disordered phase when a chiral block was compared to its racemic (random enantiomer of each monomer) counterpart. But the lamellar phase showed identical domain sizes regardless of the conformation, suggesting that the chiral block stretched more during phase separation. These effects resulted in a decrease in the temperature of the order–disorder transition temperature (T_{ODT}), further showcasing the ability for chirality to perturb phase behavior. Yet, this shift in the ODT differs from the lamellar phase formed with the PS–PLLA system, which saw an increase in T_{ODT} . Consequently, the effects of chirality on the thermodynamics governing self-assembly are not fully understood and require further investigation.

For achiral BCPs, the order–disorder transition predicted by SCFT occurs at $(\chi N)_{\text{ODT}} = 10.495$, applicable to very long, fully flexible Gaussian chains where the two blocks have identical Kuhn lengths.²² Here, χ is the Flory–Huggins parameter describing the net repulsion between the two block chemistries (also inversely related to temperature) and N is the degree of polymerization. In the literature, several conformational metrics have been studied to rationalize the impact of polymer chain shape on the ODT. For example, in Yu et al., the decrease in radius of gyration in R_g was hypothesized to lead to two effects. The first effect destabilizes the lamellar phase due to the entropic loss arising from chain stretching required to fill the domain. The second effect stems from a decrease in R_g that lowers the invariant degree of polymerization. When accounting for compositional fluctuations near the ODT for smaller polymer chains,^{35,36} it shifts the $(\chi N)_{\text{ODT}}$ toward higher values and conversely shifts the T_{ODT} to lower values.

Another example of a conformational metric that impacts the ODT is molecular rigidity, which tends to lower the $(\chi N)_{\text{ODT}}$. In simulations, molecular rigidity occurs when a bending potential is introduced. When both blocks are treated as rigid rods, the overall loss of conformational entropy enhances the relative importance of enthalpic contributions and shifts the $(\chi N)_{\text{ODT}}$ to a significantly lower value.³⁷ In chiral BCPs, these assumptions do not strictly apply, as the persistence lengths are finite and differ only to a small extent.

Relatedly, Kozuch et al. showed that increasing the mismatch in stiffness in a polymer blend (not block copolymer) increases the free energy of the disordered phase.³⁸

Likewise, conformational asymmetry, defined as the ratio of Kuhn lengths of the two (achiral) blocks, has been shown to play a significant role in BCP phase behavior. As the ratio increases above unity, it impacts the packing of the different blocks and causes spontaneous interfacial curvature toward the block with the larger Kuhn length. This in turn is responsible for the formation and stabilization of traditionally elusive ordered morphologies, such as the σ or A15 phases.^{39,40} Yet, while this phenomena shifts ordered–ordered transition boundaries and stabilizes new morphologies, it is found to have little bearing on the ODT because the enthalpic interactions remain unperturbed.³⁹

A conformational feature unique to helical polymers is the pitch. In oSCT, a dimensionless degree of chirality is inversely proportional to the pitch (length scale of orientational twist) and results in the stabilization of the helical phase, but the impact on the phases in the vicinity of the ODT is unclear.³¹

In this work, we utilize a parametrizable, phenomenologically coarse-grained, particle-based model for chiral BCPs.⁴¹ Although chemically specific coarse-grained models for polypeptoids have been recently developed, they are still computationally challenging in simulating a melt of BCPs.^{42–44} In the phenomenological model, an entire range of conformations can be studied from random coils to rod-like to perfectly helical polymers, including everything in between. From experimentally available data, it appears that chiral BCPs tend to be comprised of semiflexible helical chains.^{21,34} Interrogation of the ODT directly is challenging because the chiral block undergoes all of the aforementioned conformational changes: radius of gyration, persistence length, and pitch, each impacting the disordered phase and ordered phases uniquely. Instead, we thoroughly investigate the disordered phase by selecting a wide range of semiflexible helical conformations and address several questions regarding the thermodynamics of a melt of chiral BCPs. In **Methodology**, we describe the interactions describing the simulation model and the details of the free energy calculation technique. In **Results and Discussion**, we examine the integrands, free energy, and entropy for the model chiral BCPs. We also examine the effective block repulsion arising from the conformational change. Upon increasing chemical disparity, we are able to compare the role of conformational differences in the thermodynamics of the disordered phase. Finally, the **conclusions** are discussed.

METHODOLOGY

Modeling Chiral Diblock Copolymers. A melt of A-*b*-B diblock copolymers in the disordered state was modeled using a parametrizable, bead–spring model for helical molecules developed by Buchanan et al.⁴¹ One monomer is roughly mapped onto one bead. The nonbonded interactions between beads are governed by the repulsive-only Weeks–Chandler–Andersen potential which takes the form of

$$U_{\text{nonbonded},ij}(r_{ij}) = \begin{cases} 4\epsilon_{ij} \left[\left(\frac{\sigma}{r_{ij}} \right)^{12} + \left(\frac{\sigma}{r_{ij}} \right)^6 \right] + \epsilon_{ij}, & r \leq 2^{(1/6)}\sigma \\ 0, & r \geq 2^{(1/6)}\sigma \end{cases} \quad (1)$$

where $\sigma = 1$ is the cutoff distance at which nonbonded interactions go to zero energy and ϵ_{ij} dictates the magnitude of repulsion between the two monomers, depending on their types.⁴⁵ In this study, the self-interaction was set to unity, $\epsilon_{AA} = k_B T = \epsilon_{BB}$, whereas the cross-interaction varied, $1k_B T \leq \epsilon_{AB} \leq 2k_B T$. A harmonic potential was used for the bonded interactions following the equation

$$U_{\text{har},ij}(r_{ij}) = K_{\text{har}}(r_{ij} - R_0)^2 \quad (2)$$

with $K_{\text{har}} = 400k_B T$ and R_0 , the equilibrium bond length, set to 0.97σ . The bond angle and dihedral potentials necessary to drive chiral conformations are present only in the B block. The bond angle potential is harmonic, taking the form of

$$U_{\text{angle},ijk}(\theta_{ijk}) = K_{\theta}(\theta_{ijk} - \theta_0)^2 \quad (3)$$

where K_{θ} is the energetic parameter, θ_{ijk} is the bond angle formed between three monomers with sequential indices i , j , and k , and θ_0 is the equilibrium angle that minimizes the potential energy. The dihedral potential is a modified CHARMM potential⁴⁶ and is given by

$$U_{\text{dihedral},ijkl}(\phi_{ijkl}) = K_{\phi}[1 + \cos(\phi_{ijkl} - \phi_0)] \quad (4)$$

where K_{ϕ} is the energetic parameter, ϕ_{ijkl} is the dihedral angle between sequential monomers i , j , k , and l . Minimization of the dihedral potential occurs when the cosine function approaches the value of a negative one, which occurs at an angle of 180° . Therefore, the minimization occurs at the given set point, $\phi_{ijkl} = \phi_0 \pm 180^\circ$, and not at the defined ϕ_0 .

To allow control of chirality with simply one variable, the energetic parameter governing the dihedral angle and bond angle potentials were set equal to one another: $K_{\theta} = K_{\phi} = K$. Therefore, as we increase or decrease K , we increase or decrease the chirality of the polymer chain. Therefore, the achiral block of BCP was modeled using the same Hamiltonian as that for the chiral polymers but by setting $K = 0k_B T$.

Buchanan et al. showed that by altering K^* , θ_0 , and ϕ_0 , access to a wide array of possible helical conformations is possible.⁴¹ Figure 1 shows the pitch of a helical chain as a function of equilibrium bond and dihedral angle set point for $K = 5k_B T$.

Five different sets of equilibrium set points, covering a wide range of differing bond and dihedral angle set points, were selected to ensure that a large range of chiral conformations was represented. The selected equilibrium set points are shown in Table 1 with the single chain conformations visualized with visual molecular dynamics (VMD).⁴⁷ Models 1 and 2 were specifically chosen because the ratio of the persistence length of the chiral helix to the achiral coil roughly matches some experimentally studied polypeptides.³⁴ Other models offer no correlation to experiment that we know of at the time of this writing.

Simulation Details. Particle-based molecular dynamics simulations with three-dimensional periodic boundary conditions were conducted within the framework of large-scale atomic/molecular massively parallel simulator (LAMMPS)

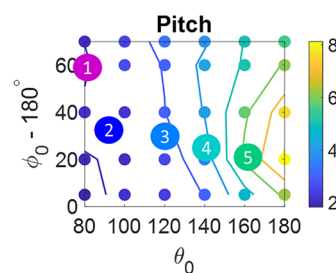


Figure 1. Pitch of a helical polymer chain in the parametrizable helical chain model at fixed $K = 5k_B T$ for several values of θ_0 and $|\phi_0 - 180^\circ|$. Each numbered circle corresponds to a specific helical model investigated in this study.

Table 1. Conformational Bonds (θ_0) and Dihedral (ϕ_0) Set Points, Equilibrium Dihedral Angles ($|\phi_0 - 180^\circ|$), Single Chain Conformation Pitches (σ), and Their Corresponding Particle-Based Conformations

Model	θ_0	ϕ_0	$ \phi_0 - 180^\circ $	Pitch (σ)	Conformation
1	80°	240°	60°	1.8969	
2	95°	145°	35°	2.1011	
3	120°	210°	30°	2.7289	
4	140°	205°	25°	3.4950	
5	160°	200°	20°	6.2111	

while using computational resources provided by Research Computing at RIT.^{48,49} The melt of diBCPs contained 250 chains, each composed of 60 monomers. The volume fraction of the chiral block (B) was $f_B = 0.5$. Simulations were performed in dimensionless units by setting $m = 1 = \sigma = k_B T$. Henceforth, variables will be reported in the dimensionless units, denoted by an asterisk. Initial equilibration of a reference disordered homopolymer melt at $K^* = K/k_B T = 0$ is outlined in the Supporting Information (SI). This reference system was used as the initial configuration to simulate each set at varying degrees of chirality ($K^* > 0$). All simulations were run in an isothermal–isobaric ensemble (NPT) at constant temperatures of $T^* = k_B T/\epsilon_{AA} = 1.0$ and $P^* = P\sigma^3/\epsilon_{AA} = 5.0$. This was implemented by two settings: a fixed isobaric–isoenthalpic (NPH) setting utilized a Nose–Hoover barostat with a damping parameter of $1000\delta t^*$, and a Langevin thermostat with a damping parameter of $100\delta t^*$. Due to the increased complexity arising from incorporation of angle and dihedral potentials, the time step was set to $\delta t^* = 0.0001$ to prevent unstable dynamics. To account for this small time step and to ensure equilibration, simulations were run for 100,000,000 time steps.

Equilibration and error analysis of each measured simulation metric was done using block averaging and is reported in 95% confidence intervals, following the prescription in Grossfield et al.⁵⁰ Block averaging was chosen as it is able to decorrelate observed parameters from previous time steps in a simulation.

Thermodynamic Integration via Gauss–Legendre Quadrature. To compute the free energy change between several model systems, we used the thermodynamic integration method. Broadly speaking, when a system can be described by

a parametrizable potential energy function $U(\lambda)$, the free energy change when λ is changed from λ_0 to λ_1 is given as^{51,52}

$$\Delta G(\lambda: \lambda_0 \rightarrow \lambda_1) = \int_{\lambda_0}^{\lambda_1} \frac{\partial G}{\partial \lambda} d\lambda = \int_{\lambda_0}^{\lambda_1} \left\langle \frac{\partial U(\lambda)}{\partial \lambda} \right\rangle_{\lambda} d\lambda \quad (5)$$

where $\langle \dots \rangle_{\lambda}$ denotes an average taken during a simulation at fixed parameter, λ . When the path $\lambda_0 \rightarrow \lambda_1$ is reversible, this equation is exact. This is expected to be particularly true in the disordered phase, where no phase transitions are observed and simple paths can be constructed. Thermodynamic integration results in a direct computation of free energy, leading to lower error bars compared to other techniques such as the evaluation of chemical potential (by particle insertion). This technique has been widely utilized in prior studies of phase diagrams of self-assembled BCPs.^{38,53,54} In order to compute this integral numerically, a quadrature scheme that converts the integral to a summation can be applied. It turns out that the second derivative of the free energy is always negative (also known as the Gibbs–Bogoliubov inequality),⁵² and the trapezoid rule that fit a zero-curvature interpolant systematically introduces error by overestimating the integral. Instead, several quadrature schemes of the form $\Delta G(\lambda: \lambda_0 \rightarrow \lambda_1) = \sum_{i=1}^{n_{\max}} w_i \left\langle \frac{\partial U(\lambda)}{\partial \lambda} \right\rangle_{\lambda_i}$ are

applicable, where n_{\max} is the number of evaluation points or nodes. Essentially, these introduce polynomial approximations with prescribed weights w_i . In this work, the Gauss–Legendre quadrature is chosen for several reasons described in Padmanabhan et al.,⁵⁴ including ease of error estimation and adaptability to irreversible, order–disordered transitions.

In this article, multiple thermodynamic integration paths are chosen (i.e., λ is mapped onto multiple variables) and the free energy changes along those paths are computed. A schematic is shown in Figure 2. A pathway in the horizontal direction uses

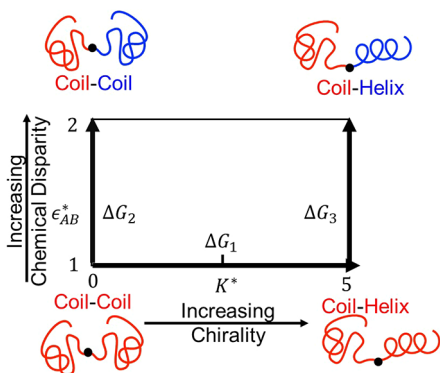


Figure 2. Free energy paths. ΔG_1 represents the change in free energy of changing the conformations of one block of the BCP. ΔG_2 measures the change in free energy of increasing chemical disparity between the two coil blocks. ΔG_3 captures the free energy change upon the introduction of chemical disparity for the coil–helix systems.

K^* as the parameter, which can be interpreted as the change arising entirely from conformational changes with no chemical disparity between the blocks. A pathway in the vertical direction uses ϵ_{AB}^* as the parameter, which can be interpreted as the change arising by introducing chemical disparity but no significant change in conformation (ΔG_2 and ΔG_3). More

details about the variable and limits (λ_0 and λ_1) are described in the subsequent section.

To determine the optimal number of nodes to use for each free energy calculation, we performed multiple evaluations of the free energy change (specifically ΔG_1) with an increasing number of nodes (n_{\max}) per quadrature. It was found that the number of nodes required to produce accurate integration results was $n_{\max} = 7$ (see the SI for more detail). A lower n_{\max} does not converge, and a higher n_{\max} results in greater overall error due to increasing of the number of terms in the summation. The typical Gauss–Legendre interval bounds are in the interval $[-1, 1]$ and are linearly shifted based on the desired bounds ($K^* = [0, 5]$ and $\epsilon_{AB}^* = [1, 2]$ in this study). Table 2 depicts the final weights and evaluation points (nodes) utilized in this study, for a typical seven-point quadrature.

Table 2. Seven-Point Gauss–Legendre Quadrature. Weights (w_i), Traditional Evaluation Points (λ_i), and Rescaled Evaluation (K_i^* and $\epsilon_{AB,i}^*$) Points after the Change of Bounds Were Applied

w_i	λ_i	K_i^*	$\epsilon_{AB,i}^*$
0.1295	−0.9491	0.1272	1.0254
0.2797	−0.7415	0.6462	1.1292
0.3818	−0.4058	1.4854	1.2971
0.4180	0	2.5000	1.5000
0.3818	0.4058	3.5146	1.7029
0.2792	0.7415	4.3548	1.8708
0.1294	0.9491	4.8728	1.9746

Integration Path: Conformational Change. To compute the free energy change due to a conformational change, the total potential energy can be expressed as being parametrized by K^* :

$$U(K) = U_{\text{nonbonded}} + U_{\text{bonded}} + K[(\theta - \theta_0)^2 + 1 + \cos(\phi - \phi_0)] \quad (6)$$

The thermodynamic path begins at the reference state, which is the random coil at $K^* = 0$ and ends at a semiflexible helical chain, obtained at a value of $K^* = 5$. Since K^* describes the parameter that drives the conformational change, the change in free energy of a helical polymer with respect to a random coil is given by

$$\begin{aligned} \frac{\Delta G_1}{nk_B T} (\epsilon_{AB}^* = 1; K^*: 0 \rightarrow 5) \\ = \int_0^5 \langle [(\theta - \theta_0)^2 + 1 + \cos(\phi - \phi_0)] \rangle_{K^*} dK^* \end{aligned} \quad (7)$$

where n is the number of monomers in the system.

Integration Path: Chemical Disparity. Chemical disparity is introduced into the system through enhancing the repulsion between dissimilar blocks by increasing ϵ_{AB}^* from unity. To compute the free energy due to increasing chemical disparity, the total potential energy can now be expressed as being parametrized by ϵ_{AB} :

$$\begin{aligned} U(\epsilon_{AB}) = \epsilon_{AB} \left(4 \left[\left(\frac{\sigma}{r_{ij}} \right)^{12} + \left(\frac{\sigma}{r_{ij}} \right)^6 \right] + 1 \right) + U_{\text{bonded}} + U_{\text{angles}} \\ + U_{\text{dihedrals}} \end{aligned} \quad (8)$$

The resulting free energy change from increasing ϵ_{AB} is directly proportional to the Flory–Huggins interaction parameter, χ .⁵⁵ The proportionality constant can be resolved but is not necessary to predict the direction of the shift in ODT.

From Figure 2, two vertical paths are constructed. The one on the left (ΔG_2) concerns the coil–coil BCP system. By setting $K^* = 0$ and increasing ϵ_{AB}^* from 1 \rightarrow 2 the free energy change of a traditional coil–coil BCP, $\chi_{\text{coil-coil}}$, can be calculated. Since our simulations occur at modest chain lengths, corrections for fluctuations must be applied. For $N = 60$ in our study, we estimated $\bar{N} \equiv \frac{216n^2R_g^6}{N^2V^2} \approx 140$. For $\epsilon_{AB}^* = 2$, correlations in Medapuram et al.⁵⁵ were used to obtain a value of $\chi N \approx 15.1$, well below $(\chi N)_{\text{ODT}} \approx 26$ for this system. Therefore, constraining the bounds of integration to [1,2] ensures a reversible thermodynamic path that remains within the disordered phase, and any possibility of a phase transition is avoided. Structure factor calculations were also conducted to verify that the integration path remained well within the disordered phase, and the details regarding these calculations can be found in the Supporting Information. Thus, $\chi_{\text{coil-coil}}$ can be calculated as

$$\begin{aligned} \chi_{\text{coil-coil}} &\propto \frac{\Delta G_2}{nk_B T} (\epsilon_{AB}^*: 1 \rightarrow 2, K^* = 0) \\ &= \int_1^2 \left\langle 4 \left[\left(\frac{\sigma}{r_{ij}} \right)^{12} + \left(\frac{\sigma}{r_{ij}} \right)^6 \right] + 1 \right\rangle_{\epsilon_{AB}^*, K^*=0} d\epsilon_{AB}^* \end{aligned} \quad (9)$$

The vertical path on the right (denoted by ΔG_3 in Figure 2) is the free energy change of the coil–helix BCP when chemical disparity is introduced, $\chi_{\text{coil-helix}}$. By taking each model investigated at $K^* = 5$ and increasing ϵ_{AB} from 1 \rightarrow 2, this free energy for the helical BCP can be calculated as

$$\begin{aligned} \chi_{\text{coil-helix}} &\propto \frac{\Delta G_3}{nk_B T} (\epsilon_{AB}^*: 1 \rightarrow 2, K^* = 5) \\ &= \int_1^2 \left\langle 4 \left[\left(\frac{\sigma}{r_{ij}} \right)^{12} + \left(\frac{\sigma}{r_{ij}} \right)^6 \right] + 1 \right\rangle_{\epsilon_{AB}^*, K^*=5} d\epsilon_{AB}^* \end{aligned} \quad (10)$$

By ensuring that both integration paths follow the same bounds of ϵ_{AB}^* , the resulting difference in free energies will be proportional to the differences in the Flory–Huggins parameter. That is, $\frac{\Delta G_3}{nk_B T} - \frac{\Delta G_2}{nk_B T} \propto \chi_{\text{coil-helix}} - \chi_{\text{coil-coil}}$. This is useful because it will measure the role of conformational changes as the spectral ODT is being approached. If this value is positive, then the polarity of the ODT is anticipated to shift to higher temperatures. If this value is negative, then the ODT is anticipated to shift to lower temperatures.

RESULTS AND DISCUSSION

In this section, we first begin by conducting the thermodynamic integration for chemically identical blocks while changing the conformation of the B block from coil to helix. We compute the free energy change for each model chiral BCP defined in Table 1. From this, the breakdown of contributions to the free energy (integrand and entropy change) is obtained, and the behavior for each model is analyzed. Then, changes in

effective block repulsions rising from the conformational changes are quantified, showing diverging thermodynamic effects for the distinct models. Further, several conformational metrics are evaluated, and we identify the primary metric that correlates with the enthalpic changes. Finally, a second thermodynamic integration is performed for the introduction of chemical mismatch between the two blocks, which also shows divergent thermodynamics that depends on the details of the chiral polymers.

Free Energy Calculations. We evaluate the free energy change between the coil homopolymer and the chiral BCP as described in Methodology for each model chiral BCP. The reference state is equivalent to a homopolymer since the blocks are chemically and conformationally identical. In Figure 3, the

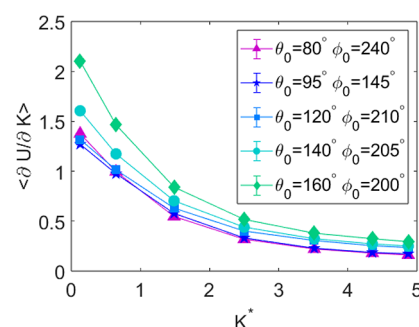


Figure 3. Integrand of the potential energy function at varying values of K^* for each model investigated in this study. Error bars are smaller than the marker sizes.

derivative of the free energy, or, equivalently, the integrand in the right-hand side of eq 7, is plotted at the Gauss–Legendre evaluation points in Table 2 for each model chiral BCP. As K_i^* is increased, the integrand decreases. Mathematically, since the integrand is equivalent to the derivative of free energy (eq 7), this also implies that the second derivative of the free energy (obtained from the slope of this curve) is negative, agreeing with the Gibbs–Bogoliubov inequality.⁵² Physically, this is explained by considering that the molecules do not follow the angular and dihedral set points at low K^* , thereby resulting in large values of the integrand (i.e., $\langle (\theta - \theta_0)^2 + 1 + \cos(\phi - \phi_0) \rangle$). At higher K^* , fewer residues deviate from the set point, resulting in smaller values of the integrand. From the graph, it is also apparent that the slope approaches zero near $K^* = 4.87$, suggesting that the block is sufficiently chiral and that a further increase in K^* is unnecessary.

Differences in the integrand across models are also evident from Figure 3. These differences are a result of how the bond and dihedral angle distributions at $K^* = 4.87$ differ from the reference state at $K^* = 0$. The origin of these differences can be discerned if we break down the contributions arising from the dihedral angles and the bond angles. The black curve in Figure 4a shows a uniform distribution of the dihedral angles for the homopolymer ($K^* = 0$). As K^* is increased, the distribution shifts toward a peaked distribution centered around the dihedral set point, $\phi_0 - 180^\circ$. The shape of the distribution is essentially the same for all models; therefore, the resulting integrand is expected to be relatively the same, as confirmed by Figure 4b. The minor differences in the dihedral contribution can be attributed to the slightly broader distributions of models 3, 4, and 5 relative to models 1 and 2. On the other hand, the bond angle distribution for the reference state is not uniform.

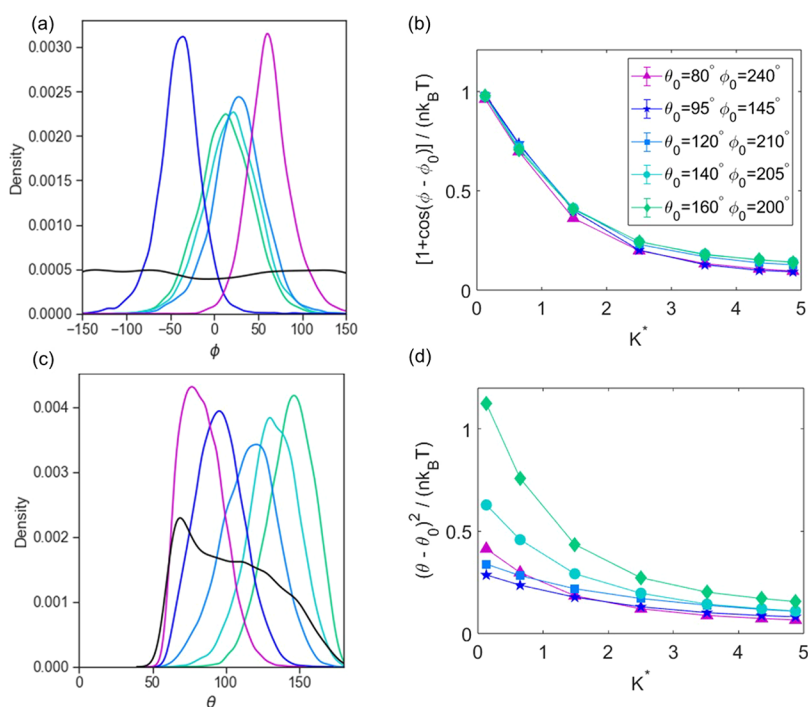


Figure 4. (a) Dihedral angle distributions in colored lines for different chiral models and in black for the achiral homopolymer. (b) Contribution to the integrand from the dihedral angle for each model. (c) Bond angle distributions in colored lines for different chiral models and in black for the achiral homopolymer. (d) Contribution to the integrand from the bond angle for each model. Legend in panel b common to all panels.

It is skewed and peaks at $\theta \approx 75^\circ$ (Figure 4c). We attribute the skewness to the steric repulsion between atoms, which excludes very small bond angles from the distribution. The distribution of the final state (i.e., coil–helix BCP) is peaked at the equilibrium angular set point. Thus, depending on the model set points, the change in the angular distribution will be different, which will result in different contributions to the integrand. Angular set points that are farther away from the peak value of the reference state will lead to a larger integrand, while set points that are closer to the peak value of the reference state will lead to smaller integrands, evident from Figure 4d. Therefore, the integrands and the free energy change depend strongly on the model chiral BCP (i.e., details of the chiral conformation). Specifically, significant shifts in bond angle distributions relative to the homopolymer result in larger integrand values.

From the integrand, the predefined quadrature schemes are applied to obtain the change in free energy for each model. In simulation, the enthalpy can be computed in a straightforward manner, which also yields the change in entropy for each model chiral BCP, using the equation below:

$$\Delta S = \frac{\langle \Delta H \rangle - \Delta G}{T} \quad (11)$$

These thermodynamic quantities are plotted in Figure 5.

All model BCPs witnessed a model-dependent increase in the free energy and enthalpy coupled with a decrease in entropy. The magnitude of the enthalpic gain is smaller compared to the entropic loss. The enthalpic gain itself arises from introducing energy into the system as K^* that imposes the governing bond and dihedral angles, and by itself, it cannot be unambiguously interpreted. However, the decrease in entropy is substantial in magnitude and can be interpreted as

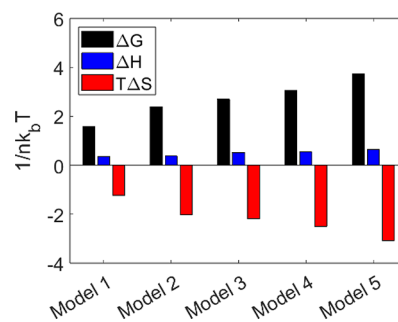


Figure 5. Resulting free energy calculations across all model chiral BCPs. Black bars represent the change in free energy per monomer, blue bars depict the change in enthalpy per monomer, and red bars show the change in entropy per monomer.

arising from the restriction of dihedral and bond angles to their equilibrium values.

As can be expected, the change in entropy is distinct for each model of BCP. The rationale behind this stems from the difference in the predefined equilibrium bond angles for each model. To maintain a desired bond angle the third monomer in the defined bond angle must occupy locations in space that are represented by the circumference of a circle imposed on a sphere with a radius of $r_\theta = b \sin(\theta_0)$, where r_θ is the radius, b is the bond length, and θ_0 is the equilibrium bond angle for each system. Conformational entropy is maximized when the radius is maximized, which occurs for $\theta_0 = 90^\circ$. Figure 6a illustrates this idea of how the bond angle impacts the number of available conformations for the molecule. The reference bond is shown in black, and the available conformations for a given angular set point are given by the band, colored by the model.

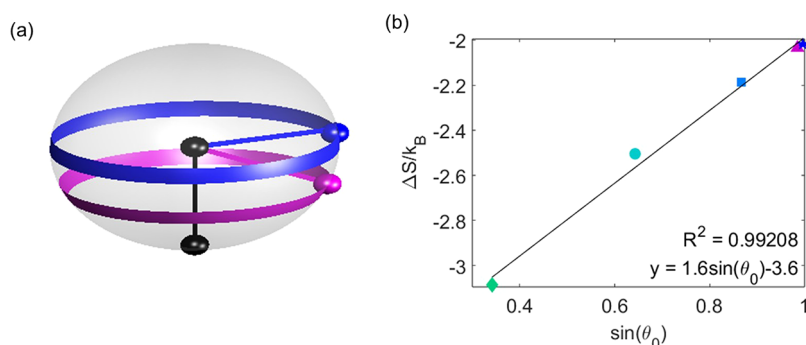


Figure 6. (a) Representation showing how decreasing the bond angle decreases the circumference of a circle around a sphere resulting in a lower number of possible configurations for the monomers associated in that bond angle. (b) Change in entropy plotted against $\sin(\theta_0)$.

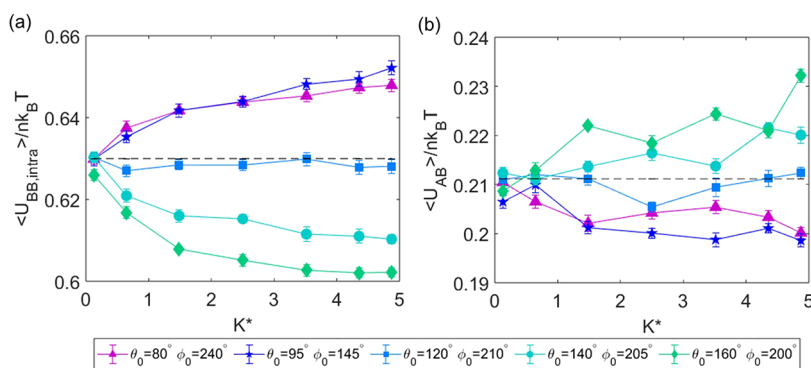


Figure 7. Divergent molecular interactions from coil–helix BCPs. This behavior is dependent on model set points leading to either an increase or decrease in helix–helix intramolecular interactions when comparing to the reference coil–coil homopolymer intramolecular interactions (a). Same divergent behavior observed between all helix–coil interactions (b).

We hypothesized that the entropy change should be related in a simple relationship to $\sin \theta_0$ that is proportional to the surface area of the band. In Figure 6b, the change in entropy is plotted against $\sin \theta_0$, and a strong correlation with a straight line is found. The equation for the line is $\frac{\Delta S}{nk_B} = 1.6 \sin(\theta_0) - 3.6$. Interestingly, if the degrees of freedom are maximized with a bond angle of 90° , the entropy loss is -2.0 . This constant value must arise from the model-independent contribution from the restricted dihedral angles.

To summarize, the significant loss of entropy in the chiral BCPs drives the increase in free energy for all model BCPs studied. The contribution stemming from the dihedral angles appears to be relatively constant across the distinct models, even though the dihedral set points are distinct. Rather, the imposed bond angles, θ_0 , significantly impact the entropy change for each model, which was found to follow a simple correlation with $\sin \theta_0$. While the alterations to entropy are a significant contributor to the free energy change, the resulting conformational changes will lead to differences in the enthalpic contributions, as well.

Enthalpic Interactions. Although each model had distinct free energy change and entropy loss, no divergence was observed; i.e., every chiral model had a higher free energy driven by a loss of entropy. This fails to explain the disparity in the ODT shifts observed in disparate experimental model chiral BCPs. So, any divergent behavior will likely occur due to enthalpic interactions. From Figure 5, it is apparent that the magnitude of the enthalpic contributions is small and positive. Subtracting the contribution arising from imposing angles and dihedrals, i.e., from increasing K^* , an even smaller magnitude

of enthalpic change is observed (see Supporting Information Figure S2).

To probe subtle changes in enthalpic interactions arising from conformational changes, intrablock interactions for the chiral block are plotted in Figure 7a and the effective block repulsion between all A-type and B-type monomers (i.e., $\langle U_{AB} \rangle / nk_B T$) are plotted in Figure 7b. The reference values for homopolymers are shown as a black dotted line. Interestingly, the chiral–chiral intrablock interactions show model-dependent divergent behavior, where the value decreases for models 1 and 2, stays nearly the same for model 3, and increases for models 4 and 5. These differences are indicative of the effects of the disparate conformations (see Table 1) adopted by the different chiral models. Therefore, the specific characteristics of the helix play a significant role. The effective block repulsion also exhibits divergent behavior. Even though the magnitude of the effective block repulsion is relatively small, it is particularly important, as it captures the energy associated with the dissimilar blocks coming into contact with one another, which is a strong driving force for phase separation. One can speculate that a lower effective block repulsion strengthens the disordered phase, leading to a lower $(\chi N)_{ODT}$ and higher T_{ODT} . A higher effective block repulsion would lead to the opposite effect. When chemical disparity is also considered, these small differences are expected to be further amplified, which will impact the ODT in different directions and to different degrees depending on the conformational details.

To develop a physical understanding and a quantitative relationship between conformational changes and effective block repulsion, we examine several conformational metrics. As outlined in the Introduction, several conformational metrics

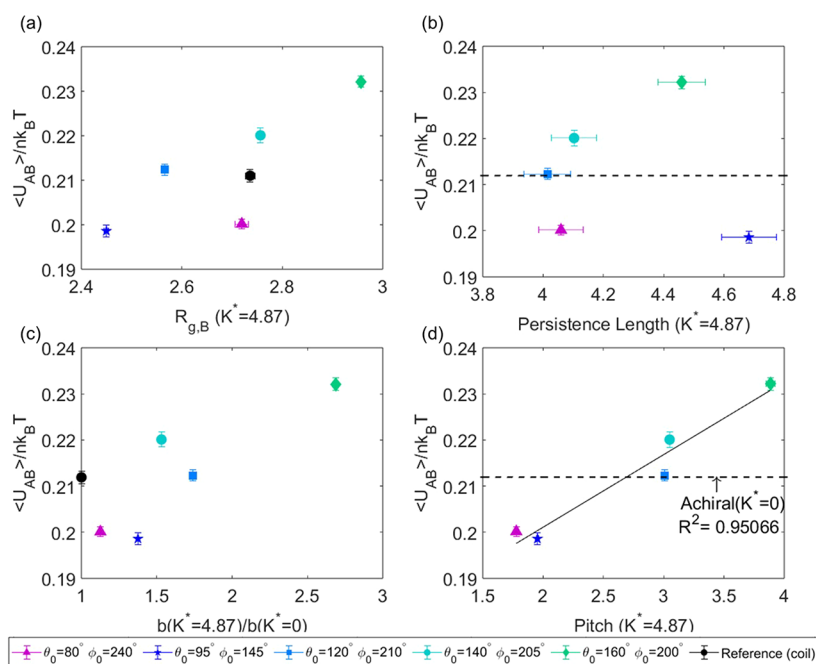


Figure 8. Effective block repulsion as a function of the radius of gyration of the helical block (a), persistence length (b), conformational asymmetry (c), and pitch (d).

have been proposed to explain the shift in the ODT for flexible or semiflexible BCP systems. Here, we summarize only the relevant aspects that would impact the disordered phase. The radius of gyration is capable of shifting the ODT in either direction due to fluctuation effects. The correction depends on the invariant degree of polymerization, \bar{N} , which scales as R_g .^{6,34–36} Stiffer chains with higher persistence length lower the relative importance of entropy.^{37,38} Conformational asymmetry, measured as the ratio of Kuhn lengths, does not tend to affect the disordered phase.^{39,40} We examine all three conformational metrics below. For helical polymers, pitch is an additional unique factor that can influence the conformation (see Figure 1 and Table 1) and will therefore be the fourth factor to be considered. Details and procedures for calculating the conformational metrics extracted from the simulations can be found in the Supporting Information or in Buchanan et al.⁴¹

In Figure 8a we plot the effective block repulsion against the radius of gyration of the B block, $R_{g,B}$. Relative to the random coil indicated by the black dot, $R_{g,B}$ exhibits two diverging regimes (i.e., compressed and extended). One expects that as the size of the block increases, the propensity to interact with neighboring molecules will also increase. Therefore, helical polymers that have a smaller radius of gyration than the reference coil blocks are expected to have decreased interactions with neighboring chains or, equivalently, a lower value of $\langle U_{AB} \rangle$. This decrease in $\langle U_{AB} \rangle$ would stabilize the disordered phase and lower the order–disorder transition temperature, much like what was observed by Yu et al. due to ordered phase destabilization. Specifically, parameters in models 1 and 2 closely match the reported values in the experimental literature (number of monomers per turn and persistence length ratios),^{34,41} and our data qualitatively match experimental findings of lower $R_{g,B}$ in the disordered phase.³⁴ Our data also predict that chiral BCPs corresponding to other models (4 and 5) would result in the opposite thermodynamic behavior of increasing T_{ODT} . But, we also note that this correlation between $R_{g,B}$ and $\langle U_{AB} \rangle$ is not universal across all

the models. For example, model 3 shows a decrease in $R_{g,B}$ accompanied by an increase in $\langle U_{AB} \rangle$.

We believe that the radius of gyration is not the appropriate metric for describing the conformations in the disordered state because of the inherent assumption that the helical block maintains a spherical shape. To test the departure from a spherical conformation, we examined the full R_g tensor and calculated the asphericity, anisotropy, and acylindricity of the system (see the SI for the equations), shown in Table 3. Lower

Table 3. Asphericity, Anisotropy, \bar{N} , and Acylindricity for the Reference BCP and Each Model

Model	Asphericity	Anisotropy	\bar{N}	Acylindricity
Coil	0.204	0.001	143.81	0.227
1	2.678	0.159	165.94	1.866
2	2.932	0.217	132.61	1.378
3	3.086	0.177	132.34	1.637
4	1.621	0.092	146.46	1.249
5	3.064	0.171	183.48	1.412

values of asphericity and anisotropy indicate a spherical shape, while low values of acylindricity indicate a cylindrical shape. The coil block (reference state in the free energy calculation) has an asphericity of 0.204 and an anisotropy of 0.001, confirming that it is nearly isotropic and takes on a spherical conformation. The helical blocks for all models have asphericity values between 1.621 and 3.064 with anisotropy measurements nearly 2 orders of magnitude greater than the coil–coil reference state, indicating a nonspherical conformation. This large deviation in anisotropic evaluation renders simply using the R_g as ineffective for capturing the effects of changing conformation on $\langle U_{AB} \rangle$, as the detail of the conformation is not captured from this simple metric. Since the radius of gyration is known to affect the extent of fluctuation corrections in flexible BCPs, we also computed the

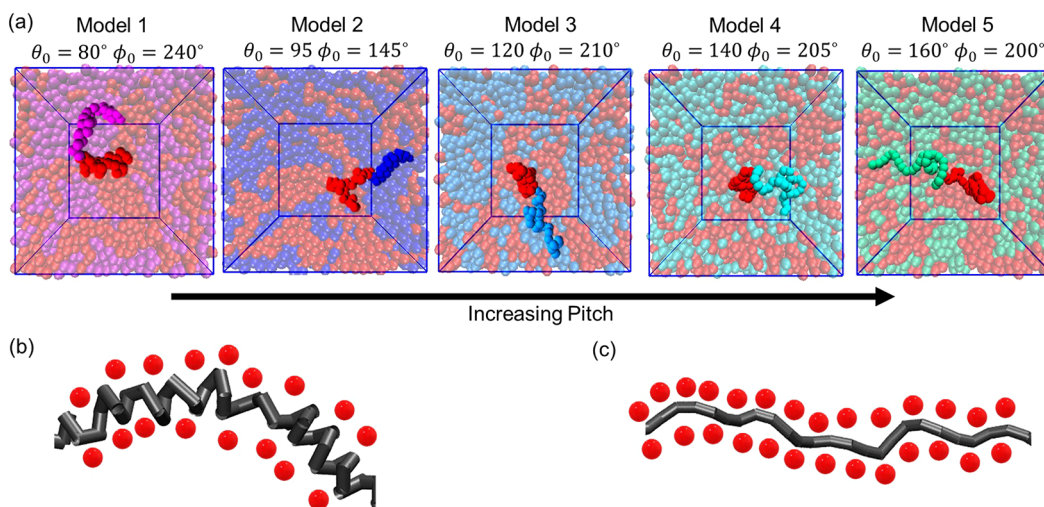


Figure 9. (a) Particle-based conformations of helical BCP chains for each model investigated in this study. (b) Physical representation of a helical block containing a small pitch. Possible matrix contacts pictured in red are unable to access the inner portion of the helix. (c) Helical block with a larger pitch, which is more accessible to its surrounding matrix.

invariant degree of polymerization and found that these values changed across the models. But due to the anisotropy, considering the effect of fluctuations is not straightforward.

Another useful anisotropic metric is the acylindricity, which is the difference between the two smallest eigenvectors of the gyration tensor. Physically speaking, a spherical projection perpendicular to the primary axis would result in low acylindricity, while an elliptical projection would result in high acylindricity. The high values of acylindricity (Table 3) indicate that the helical conformations are not cylindrical but are semiflexible. Thus, the conformational changes do not resemble the transition from a coil-like to a rigid and elongated helix. Therefore, persistence length is also poorly correlated with effective block repulsion, as observed in Figure 8b. Thus, theoretical predictions from the literature which predicts a higher incompatibility for greater stiffness mismatch are not strictly applicable.^{37,38}

Next, we investigated the role of conformational asymmetry defined as the ratio of Kuhn lengths of the helical and coil blocks. For coil blocks, the Kuhn length is proportional to the persistence length, but due to the anisotropy inherent in the helical blocks, the Kuhn length is computed independently using chain statistics, as outlined in the Supporting Information, and conformational asymmetry is plotted in Figure 8c. At low conformational asymmetry, a decrease in $\langle U_{AB} \rangle$ is observed, whereas, at higher values, it increases. This non-monotonic behavior shows that conformational asymmetry fails to capture the molecular interactions of helical polymers.

From parts a–c of Figure 8, it is apparent that typical conformational metrics used to describe coil-like or rod-like families of BCPs, do not transfer well to helical models. Thus, existing theoretical predictions relying on fluctuation corrections or chain stiffness cannot be directly applied to chiral BCPs. This is because each of the metrics fails to capture an important detail novel to helical blocks: pitch. Yamakawa⁵⁶ used the parameters in a continuous helical equation to connect various polymer conformations by tuning the pitch parameter. In the limit of infinite pitch, the rigid rod model is observed, while in the limit of zero pitch it becomes a planar spiral. By choosing our model set points, we capture realistic

helical conformations that are semiflexible and of varying pitch (see Table 1). When pitch is compared to $\langle U_{AB} \rangle$ a strong linear correlation is found as observed in Figure 8d. A higher pitch results in an increase in $\langle U_{AB} \rangle$, whereas a lower pitch decreases it. The coil block for which the pitch is not defined appears to fall in the intermediate range of our chosen models.

To physically understand why the effective block repulsion depends on the pitch, we examined the simulation snapshots. Figure 9a highlights some representative conformations of the isolated molecules for each model. The red beads in this panel represent the achiral, “A” block, while the varying colors (purple, blue, and green) represent the chiral, “B” blocks. The reported variation in the conformation (radius of gyration, flexibility, and pitch) can be qualitatively observed. In particular, the B block appears to elongate from the left to right. This elongation appears to be subtle as the pitch for each system ranges from 2σ to 6σ . The smaller pitches tend to exclude a significant number of monomers from interacting with the surrounding molecules (models 1 and 2). This inaccessible region decreases the number of net contacts between the polymer and its surrounding matrix. This is captured in Figure 9b, where the inside of the tightly coiled helix is inaccessible to the red spheres (used to represent matrix contacts). As the pitch increases, the helix becomes more exposed, increasing the ability for surrounding molecules to come into contact with it (Figure 9c). The random coil will tend to have an intermediate value of contact, as seen by the achiral reference line in Figure 8d. Therefore we see that rather than traditional conformational metrics, the characteristics of the helix play a significant role in rationalizing the divergent effective block repulsions displayed for the different helical models relative to the (achiral) coiled homopolymer.

We note that the critical role that pitch plays on chiral BCP thermodynamics has been brought up in previous work.³² However, in oSCFT, the pitch refers to the length scale over which the molecules twist and is normalized by the end-to-end distance of the molecule. In this work, pitch denotes the length scale over which the intramolecular conformation twists relative to the bead diameter. Establishing the connection between the two is beyond the scope of this work.

Nevertheless, it appears that pitch drives the thermodynamic behavior of chiral BCPs on multiple length scales.

To summarize, for the chemically identical blocks, depending on the model system, effective block repulsion $\langle U_{AB} \rangle / nk_B T$ exhibits divergent behavior. All of the examined conformational metrics also examined divergent behavior in comparison to the homopolymer. Yet, the semiflexible and helical nature of the molecules led to poor quantitative correlation between the radius of gyration, persistence length, and Kuhn length. Instead, the characteristic conformational parameter for helices, i.e., pitch, resulted in a strong correlation with effective block repulsion. Next, we explore how the varying helical conformations impact the change in free energy when chemical disparity between blocks is increased.

Effects of Introducing Chemical Disparity. The free energy change when increasing the chemical incompatibility (disparity) between the two blocks is related to the Flory–Huggins interaction parameter χ for coil–coil systems. A similar pathway can be constructed for increasing the chemical incompatibility by the same amount for the coil–helix systems (Figure 2). The magnitude of chemical incompatibility (ϵ_{AB}^*) is chosen to remain in the disordered state and maintains reversibility. As described in Methodology, the difference between the latter and the former is plotted in Figure 10 and is

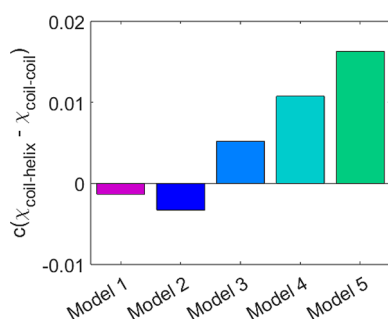


Figure 10. Changes in χ between coil–helix models and the reference coil–coil analogue.

proportional to $\chi_{\text{coil-helix}} - \chi_{\text{coil-coil}}$. Note that, in this plot, we have not resolved the proportionality constant c and we comment only on the sign rather than the magnitude, which provides insight as to how the helical conformations impact the free energy of the disordered state. The individual contributions of $\Delta G_2 / nk_B T$ and $\Delta G_3 / nk_B T$ computed from eqs 9 and 10 are shown in Figure S3. For models 1 and 2 with smaller pitch, a negative shift in $\Delta\chi$ is observed, which indicates that the chiral BCP is more stable in the disordered phase compared to the coil–coil analogue. This result is in agreement with the experimental result by Yu et al. where the Flory–Huggins parameter for the coil–helix BCP was lower than the coil–coil BCP.³⁴ For models 3, 4, and 5 with a larger pitch, a positive shift in χ is observed. This divergence further shows that the pitch-based divergence in thermodynamics in the effective block repulsion extends when chemical disparity is increased.

CONCLUSIONS

Using particle-based simulations, a melt of coil–helix block copolymers in the disordered phase was studied. Five different models of coil–helix BCPs were chosen that varied in the pitch of the helix. Among these, models 1 and 2 have conformational

metrics that are similar to recently reported experimental conformations by chiral BCPs.³⁴ To understand the details of the thermodynamics, the free energy change was computed along three different paths. In path 1 the blocks were chemically identical, while the conformation of the B block was changed from a coil to a helix. In path 2, the blocks were conformationally identical (coil–coil), while the chemical disparity between the blocks was increased. In path 3, the blocks were conformationally distinct (coil–helix) and the chemical disparity was increased.

The largest change in free energy is associated with path 1, which is mainly driven by a substantial decrease in entropy. This large decrease in entropy is attributed to the restriction of the dihedral and bond angles to their equilibrium set points during the formation of helical conformations. While the dihedral angle contributions were relatively constant for each model, the bond angle contributions are model-dependent. This dependence was quantified and is found to be related to $\sin(\theta_0)$, which is simply the surface area of accessible conformations on a sphere when bond angles are restricted to θ_0 .

Despite having chemically identical blocks along path 1, the conformational changes exhibit divergent enthalpic contributions relative to the coil homopolymer. This suggests that the introduction of chirality into a block does not fully capture the thermodynamic effects, but the characteristics of the helix play a significant role in the thermodynamics of these systems. Particularly, the effective block repulsion, an important driving force for phase separation, decreases in some models and increases in others. Conformational metrics such as the radius of gyration and conformational asymmetry also exhibit model-dependent divergent behavior but do not quantitatively describe the effective block repulsion. We argue that the nature of the helices cannot be simply described as spherical, coil-like, nor rod-like, and thus, characteristic metrics typically used in flexible or stiff BCPs do not capture the behavior. Instead, we found that the metric indicative of chirality, i.e., the pitch, is best correlated with effective block repulsions. Shorter pitch results in lower effective block repulsion, and longer pitch results in higher effective block repulsion.

Subsequently, the free energy change was computed for increasing the chemical disparity between the blocks. The difference between free energies from paths 3 and 2 is also proportional to the difference in Flory–Huggins parameter $\chi_{\text{coil-helix}} - \chi_{\text{coil-coil}}$. We found that models with helical polymers possessing smaller pitches exhibit a negative shift in χ , whereas those with larger pitches undergo a positive shift in χ .

Throughout this work, results for models 1 and 2 (radius of gyration and $\Delta\chi$) are consistent with experimentally reported observations in the disordered phase, which resulted in a lower T_{ODT} for PnBA-*b*-polypeptoid.³⁴ However, experimental observations on an alternate chemistry (PS-*b*-PLLA) exhibited a higher T_{ODT} for the chiral BCP. Although the cause for the shift in the level of ODT cannot be identified from the disordered phase alone, our results suggest that chiral block copolymers exhibit unique thermodynamics in the disordered phase that strongly depend on the pitch of the molecule. In fact, the changes in pitch across models 1, 2, and 3 differ by less than one monomer diameter. These distinct conformations could be potentially accessed by changing the chemical groups attached to the backbone.

■ ASSOCIATED CONTENT

SI Supporting Information

The Supporting Information is available free of charge at <https://pubs.acs.org/doi/10.1021/acs.jctc.3c00680>.

Initialization of disordered reference melt; Gauss–Legendre quadrature optimization; enthalpic contributions in ΔG_1 ; radius of gyration tensor; Kuhn lengths calculations; free energy calculations; structure factors (PDF)

■ AUTHOR INFORMATION

Corresponding Author

Poornima Padmanabhan – *Microsystems Engineering, Rochester Institute of Technology, Rochester, New York 14623, United States; Department of Chemical Engineering, Rochester Institute of Technology, Rochester, New York 14623, United States;* orcid.org/0000-0001-9445-1723; Email: poornima.padmanabhan@rit.edu

Authors

Michael J. Grant – *Microsystems Engineering, Rochester Institute of Technology, Rochester, New York 14623, United States;* orcid.org/0000-0002-8322-803X

Brennan J. Fingler – *Department of Chemical Engineering, Rochester Institute of Technology, Rochester, New York 14623, United States*

Natalie Buchanan – *Microsystems Engineering, Rochester Institute of Technology, Rochester, New York 14623, United States;* orcid.org/0000-0003-1114-7801

Complete contact information is available at: <https://pubs.acs.org/doi/10.1021/acs.jctc.3c00680>

Notes

The authors declare no competing financial interest.

■ ACKNOWLEDGMENTS

We thank Dr. Emiliano Brini, Dr. Rong-Ming Ho, and Dr. Joshua Lequieu for helpful discussions. Funding support from the National Science Foundation DMR-2144511 and the Kate Gleason College Fund are gratefully acknowledged. We also thank Research Computing at RIT for computational resources and support in compiling and managing software libraries utilized in this work.

■ REFERENCES

- (1) Yashima, E.; Ousaka, N.; Taura, D.; Shimomura, K.; Ikai, T.; Maeda, K. Supramolecular Helical Systems: Helical Assemblies of Small Molecules, Foldamers, and Polymers with Chiral Amplification and Their Functions. *Chem. Rev.* **2016**, *116*, 13752–13990.
- (2) Scanga, R. A.; Reuther, J. F. Helical polymer self-Assembly and chiral nanostructure formation. *Polym. Chem.* **2021**, *12*, 1857–1897.
- (3) Xia, Q.; Meng, L.; He, T.; Huang, G.; Li, B. S.; Tang, B. Z. Direct Visualization of Chiral Amplification of Chiral Aggregation Induced Emission Molecules in Nematic Liquid Crystals. *ACS Nano* **2021**, *15*, 4956–4966.
- (4) Azeroual, S.; Surprenant, J.; Lazzara, T. D.; Kocun, M.; Tao, Y.; Cuccia, L. A.; Lehn, J.-M. Mirror Symmetry Breaking and Chiral Amplification in Foldamer-based Supramolecular Helical Aggregates. *Chem. Commun.* **2012**, *48*, 2292–2294.
- (5) Anderson, T. W.; Sanders, J. K. M.; Pantos, G. D. The Sergeants-and-Soldiers Effect: Chiral Amplification in Naphthalenediimide Nanotubes. *Org. Biomol. Chem.* **2010**, *8*, 4274–4280.

- (6) Zhang, L.; Wang, T.; Jiang, J.; Liu, M. Chiral Porphyrin Assemblies. *Aggregate* **2023**, *4*, e198.
- (7) Toyofuku, K.; Alam, M.; Tsuda, A.; Fujita, N.; Sakamoto, S.; Yamaguchi, K.; Aida, T. Amplified Chiral Transformation through Helical Assembly. *Angew. Chem., Int. Ed.* **2007**, *46*, 6476–6480.
- (8) Helmich, F.; Smulders, M. M. J.; Lee, C. C.; Schenning, A. P. H. J.; Meijer, E. W. Effect of Stereogenic Centers on the Self-Sorting, Depolymerization, and Atropisomerization Kinetics of Porphyrin-Based Aggregates. *J. Am. Chem. Soc.* **2011**, *133*, 12238–12246.
- (9) Yan, X.; Wang, Q.; Chen, X.; Jiang, Y.-B. Supramolecular Chiral Aggregates Exhibiting Nonlinear CD–ee Dependence. *Adv. Mater.* **2020**, *32*, 1905667.
- (10) Zhao, B.; Pan, K.; Deng, J. Combining Chiral Helical Polymer with Achiral Luminophores for Generating Full-Color, On-Off, and Switchable Circularly Polarized Luminescence. *Macromolecules* **2019**, *52*, 376–384.
- (11) Ahmed, W.; Karabaliev, M.; Gao, C. Taking Chiral Polymers Toward Immune Regulation. *J. Polym. Sci.* **2022**, *60*, 2213–2224.
- (12) Mondal, A. K.; Preuss, M. D.; Ślęczkowski, M. L.; Das, T. K.; Vantomme, G.; Meijer, E. W.; Naaman, R. Spin Filtering in Supramolecular Polymers Assembled from Achiral Monomers Mediated by Chiral Solvents. *J. Am. Chem. Soc.* **2021**, *143*, 7189–7195.
- (13) Reggelin, M.; Doerr, S.; Klusmann, M.; Schultz, M.; Holbach, M. Helically Chiral Polymers: A Class of Ligands for Asymmetric Catalysis. *Proc. Natl. Acad. Sci. U. S. A.* **2004**, *101*, 5461–5466.
- (14) Chen, C.-K.; Hsueh, H.-Y.; Chiang, Y.-W.; Ho, R.-M.; Akasaka, S.; Hasegawa, H. Single Helix to Double Gyroid in Chiral Block Copolymers. *Macromolecules* **2010**, *43*, 8637–8644.
- (15) Wang, H.-F.; Wang, H.-W.; Ho, R.-M. Helical Phase from Blending of Chiral Block Copolymer and Homopolymer. *Chem. Commun.* **2012**, *48*, 3665–3667.
- (16) Zhao, W.; Liu, F.; Wei, X.; Chen, D.; Grason, G. M.; Russell, T. P. Formation of H* Phase in Chiral Block Copolymers: Morphology Evolution As Revealed by Time-Resolved X-ray Scattering. *Macromolecules* **2013**, *46*, 474–483.
- (17) Higuchi, T.; Sugimori, H.; Jiang, X.; Hong, S.; Matsunaga, K.; Kaneko, T.; Abetz, V.; Takahara, A.; Jinnai, H. Morphological Control of Helical Structures of an ABC-Type Triblock Terpolymer by Distribution Control of a Blending Homopolymer in a Block Copolymer Microdomain. *Macromolecules* **2013**, *46*, 6991–6997.
- (18) Yang, K.-C.; Ho, R.-M. Spiral Hierarchical Superstructures from Twisted Ribbons of Self-Assembled Chiral Block Copolymers. *ACS Macro Lett.* **2020**, *9*, 1130–1134.
- (19) Murnen, H. K.; Rosales, A. M.; Jaworski, J. N.; Segalman, R. A.; Zuckermann, R. N. Hierarchical Self-Assembly of a Biomimetic Diblock Copolypeptide into Homochiral Superhelices. *J. Am. Chem. Soc.* **2010**, *132*, 16112–16119.
- (20) Xu, P.; Gao, L.; Cai, C.; Lin, J.; Wang, L.; Tian, X. Helical Toroids Self-Assembled from a Binary System of Polypeptide Homopolymer and its Block Copolymer. *Angew. Chem., Int. Ed.* **2020**, *59*, 14281–14285.
- (21) Davidson, E. C.; Rosales, A. M.; Patterson, A. L.; Russ, B.; Yu, B.; Zuckermann, R. N.; Segalman, R. A. Impact of Helical Chain Shape in Sequence-Defined Polymers on Polypeptide Block Copolymer Self-Assembly. *Macromolecules* **2018**, *51*, 2089–2098.
- (22) Leibler, L. Theory of Microphase Separation in Block Copolymers. *Macromolecules* **1980**, *13*, 1602–1617.
- (23) Bates, F. S.; Fredrickson, G. H. Block Copolymer Thermodynamics: Theory and Experiment. *Annu. Rev. Phys. Chem.* **1990**, *41*, 525–557.
- (24) Klok, H.-A.; Lecommandoux, S. Supramolecular Materials via Block Copolymer Self-Assembly. *Adv. Mater.* **2001**, *13*, 1217–1229.
- (25) Kim, J. K.; Yang, S. Y.; Lee, Y.; Kim, Y. Functional Nanomaterials Based on Block Copolymer Self-assembly. *Prog. Polym. Sci.* **2010**, *35*, 1325–1349.
- (26) Hu, X. H.; Xiong, S. Fabrication of Nanodevices Through Block Copolymer Self-Assembly. *Front. Nanotechnol.* **2022**, *4*, 762996.

- (27) Olsen, B. D.; Segalman, R. A. Phase Transitions in Asymmetric Rod-Coil Block Copolymers. *Macromolecules* **2006**, *39*, 7078–7083.
- (28) Ho, R.-M.; Chiang, Y.-W.; Chen, C.-K.; Wang, H.-W.; Hasegawa, H.; Akasaka, S.; Thomas, E. L.; Burger, C.; Hsiao, B. S. Block Copolymers with a Twist. *J. Am. Chem. Soc.* **2009**, *131*, 18533–18542.
- (29) Chiang, Y.-W.; Ho, R.-M.; Burger, C.; Hasegawa, H. Helical assemblies from chiral block copolymers. *Soft Matter* **2011**, *7*, 9797–9803.
- (30) Zhao, W.; Russell, T. P.; Grason, G. M. Orientational Interactions in Block Copolymer Melts: Self-consistent Field Theory. *J. Chem. Phys.* **2012**, *137*, 104911.
- (31) Zhao, W.; Russell, T. P.; Grason, G. M. Chirality in Block Copolymer Melts: Mesoscopic Helicity from Intersegment Twist. *Phys. Rev. Lett.* **2013**, *110*, 058301.
- (32) Grason, G. M. Chirality Transfer in Block Copolymer Melts: Emerging Concepts. *ACS Macro Lett.* **2015**, *4*, 526–532.
- (33) Wang, H. F.; Yang, K. C.; Hsu, W. C.; Lee, J. Y.; Hsu, J. T.; Grason, G. M.; Thomas, E. L.; Tsai, J. C.; Ho, R. M. Generalizing the Effects of Chirality on Block Copolymer Assembly. *Proc. Natl. Acad. Sci. U. S. A.* **2019**, *116*, 4080–4089.
- (34) Yu, B.; Danielsen, S. P. O.; Patterson, A. L.; Davidson, E. C.; Segalman, R. A. Effects of Helical Chain Shape on Lamellae-Forming Block Copolymer Self-Assembly. *Macromolecules* **2019**, *52*, 2560–2568.
- (35) Fredrickson, G. H.; Helfand, E. Fluctuation Effects in the Theory of Microphase Separation in Block Copolymers. *J. Chem. Phys.* **1987**, *87*, 697–705.
- (36) Glaser, J.; Medapuram, P.; Beardsley, T. M.; Matsen, M. W.; Morse, D. C. Universality of Block Copolymer Melts. *Phys. Rev. Lett.* **2014**, *113*, 068302.
- (37) Matsen, M. W. Melts of Semiflexible Diblock Copolymer. *J. Chem. Phys.* **1996**, *104*, 7758–7764.
- (38) Kozuch, D. J.; Zhang, W.; Milner, S. T. Predicting the Flory-Huggins χ Parameter for Polymers with Stiffness Mismatch from Molecular Dynamics Simulations. *Polymers* **2016**, *8*, 241.
- (39) Bates, M. W.; Lequeieu, J.; Barbon, S. M.; Lewis, R. M.; Delaney, K. T.; Anastasaki, A.; Hawker, C. J.; Fredrickson, G. H.; Bates, C. M. Stability of the A15 Phase in Diblock Copolymer Melts. *Proc. Natl. Acad. Sci. U. S. A.* **2019**, *116*, 13194–13199.
- (40) Schulze, M. W.; Lewis, R. M.; Lettow, J. H.; Hickey, R. J.; Gillard, T. M.; Hillmyer, M. A.; Bates, F. S. Conformational Asymmetry and Quasicrystal Approximants in Linear Diblock Copolymers. *Phys. Rev. Lett.* **2017**, *118*, 207801.
- (41) Buchanan, N.; Provenzano, J.; Padmanabhan, P. A Tunable, Particle-Based Model for the Diverse Conformations Exhibited by Chiral Homopolymers. *Macromolecules* **2022**, *55*, 6321–6331.
- (42) Mirijanian, D. T.; Mannige, R. V.; Zuckermann, R. N.; Whitelam, S. Development and Use of an Atomistic CHARMM-based Forcefield for Peptoid Simulation. *J. Comput. Chem.* **2014**, *35*, 360–370.
- (43) Jiao, S.; DeStefano, A.; Monroe, J. I.; Barry, M.; Sherck, N.; Casey, T.; Segalman, R. A.; Han, S.; Shell, M. S. Quantifying Polypeptoid Conformational Landscapes through Integrated Experiment and Simulation. *Macromolecules* **2021**, *54*, 5011–5021.
- (44) Zhao, M.; Sampath, J.; Alamdari, S.; Shen, G.; Chen, C.-L.; Mundy, C. J.; Pfandtner, J.; Ferguson, A. L. MARTINI-Compatible Coarse-Grained Model for the Mesoscale Simulation of Peptoids. *J. Phys. Chem. B* **2020**, *124*, 7745–7764.
- (45) Weeks, J. D.; Chandler, D.; Andersen, H. C. Role of Repulsive Forces in Determining the Equilibrium Structure of Simple Liquids. *J. Chem. Phys.* **1971**, *54*, 5237–5247.
- (46) MacKerell, A. D., Jr.; Brooks, B.; Brooks, C. L., III; Nilsson, L.; Roux, B.; Won, Y.; Karplus, M. CHARMM: The Energy Function and Its Parameterization. *Encyclopedia of Computational Chemistry*; John Wiley & Sons, 2002.
- (47) Humphrey, W.; Dalke, A.; Schulten, K. VMD – Visual Molecular Dynamics, version 1.9.3. *J. Mol. Graphics* **1996**, *14*, 33–38.
- (48) Thompson, A. P.; Aktulga, H. M.; Berger, R.; Bolintineanu, D. S.; Brown, W. M.; Crozier, P. S.; in 't Veld, P. J.; Kohlmeyer, A.; Moore, S. G.; Nguyen, T. D.; Shan, R.; Stevens, M. J.; Tranchida, J.; Trott, C.; Plimpton, S. J. LAMMPS - a Flexible Simulation tool for Particle-based Materials Modeling at the Atomic, Meso, and Continuum Scales, version 21 July 2020. *Comput. Phys. Commun.* **2022**, *271*, 108171.
- (49) Rochester Institute of Technology. *Research Computing Services*, 2023; <https://www.rit.edu/researchcomputing/> (accessed on 202308-27).
- (50) Grossfield, A.; Patrone, P. N.; Roe, D. R.; Schultz, A. J.; Siderius, D.; Zuckerman, D. M. Best Practices for Quantification of Uncertainty and Sampling Quality in Molecular Simulations [Article v1.0]. *Living J. Comput. Mol. Sci.* **2019**, *1*, 5067.
- (51) Kirkwood, J. G. Statistical Mechanics of Fluid Mixtures. *J. Chem. Phys.* **1935**, *3*, 300–313.
- (52) Frenkel, D.; Smit, B. In *Understanding Molecular Simulation*, 2nd ed.; Frenkel, D., Smit, B., Eds.; Academic Press: San Diego, 2002; pp 167–200.
- (53) Nagpal, U.; Müller, M.; Nealey, P. F.; de Pablo, J. J. Free Energy of Defects in Ordered Assemblies of Block Copolymer Domains. *ACS Macro Lett.* **2012**, *1*, 418–422.
- (54) Padmanabhan, P.; Martinez-Veracochea, F.; Escobedo, F. A. Computation of Free Energies of Cubic Bicontinuous Phases for Blends of Diblock Copolymer and Selective Homopolymer. *Macromolecules* **2016**, *49*, 5232–5243.
- (55) Medapuram, P.; Glaser, J.; Morse, D. C. Universal phenomenology of symmetric diblock copolymers near the order-disorder transition. *Macromolecules* **2015**, *48*, 819–839.
- (56) Yamakawa, H.; Yoshizaki, T. *Helical wormlike chains in Polymer Solutions*, 2nd ed.; Springer: Berlin, 2018.

Supporting Information

Coil-helix block copolymers can exhibit divergent thermodynamics in the disordered phase

Michael J. Grant,[†] Brennan J. Fingler,[‡] Natalie Buchanan,[†] and Poornima
Padmanabhan^{*,†,‡}

[†]*Microsystems Engineering, Rochester Institute of Technology, Rochester, NY*

[‡]*Department of Chemical Engineering, Rochester Institute of Technology, Rochester, NY*

E-mail: poornima.padmanabhan@rit.edu

Initialization of Disordered Reference Melt

A simulation containing 250 block copolymer chains composed of 60 monomers and chiral volume fraction of $f_B = 0.5$ were initiated in a lamellar morphology by following the procedure from Seo *et al.*¹ We note that this initial state quickly becomes disordered, and is only implemented for the sake of convenience. All dihedral and bond angle potentials were initially shut off ($K^* = 0$) while the energetic parameter governing the bond angles was set to $400k_B T$ with an equilibrium bond length of 0.97σ . To eliminate the high energetic penalty of overlapping atoms given from the initial input structure, the nonbonded interactions were initially governed by a soft potential defined as:

$$V_{soft} = A \left[1 + \cos \left(\frac{\pi r_{ij}}{r_c} \right) \right], \quad r_{ij} < r_c \quad (\text{S1})$$

where r_c is the cutoff distance for the potential, r_{ij} is the distance between two non-bonded atoms of index i and j and A is an energetic term that is identical for all particle types and incrementally increases as the simulation time increases ($A = 50 \times \frac{t^*}{1000} k_B T$). This

initial minimization was conducted utilizing the canonical (NVT) ensemble with $k_B T = 1.0$, implemented by a Nose-Hoover thermostat with a damping parameter of $100\delta t^*$. The initial pushoff was then simulated with a timestep increment of $\delta t^* = 0.005$ for 10,000 timesteps.

Once the overlapping atoms were separated, the non-bonded interactions were switched from the soft potential to the WCA potential (Equation 2 in the main text). The energetic parameter ϵ^* was set to 1 for each non-bonded interaction (AA , BB , and AB). The simulation box was then deformed to a cubic box to accommodate a monomer bead density of $0.85\sigma^{-3}$ under a microcanonical ensemble (NVE) for another 10,000 timesteps with a Langevin thermostat maintaining a temperature of $T^* = 1.0$ with damping parameter of $100\delta\tau$. Finally an isoenthalpic ensemble (NPH) was utilized with a Nose-Hoover barostat maintaining a pressure of $P^* = 5.0$ with a damping parameter of $1000\delta t^*$ and the simulation was allowed to equilibrate for another 100,000 timesteps. A disordered melt was then visualized with the VMD software package.²

This starting snapshot was used to initiate additional simulations at target K^* or ϵ_{AB}^* for 100,000,000 timesteps from which the initial 40-50% were discarded.

Gauss-Legendre Quadrature Optimization

The accuracy of a Gauss-Legendre quadrature is sensitive to the number of nodes used in the calculation. Too few nodes and the resulting integration will be erroneous while too many nodes result in excess computational requirements. Every function has an optimal number of nodes that both minimize error while being computationally cost efficient. Using Python's NumPy library weights (w_i) and scaled nodes (K_i) for quadratures ranging from 5 – 15 points were calculated. These nodes, and their subsequent weights can be found in Table S1. The resulting free energies can be observed in Figure S1.

Table S1: Gauss-Legendre quadratures tested for finding optimal number of nodes. Weights (w_i) and rescaled evaluation (K_i^*) points after the change of bounds were applied.

$w_i(5)$	$K_i^*(5)$	$w_i(7)$	$K_i^*(7)$	$w_i(9)$	$K_i^*(9)$	$w_i(11)$	$K_i^*(11)$	$w_i(13)$	$K_i^*(13)$	$w_i(15)$	$K_i^*(15)$
0.2369	0.2346	0.1295	0.1272	0.0813	0.0796	0.0557	0.0544	0.0405	0.0395	0.0308	0.0300
0.4786	1.1538	0.2797	0.6462	0.1806	0.4099	0.1256	0.2823	0.0921	0.2060	0.0704	0.1568
0.5689	2.5000	0.3818	1.4854	0.2606	0.9666	0.1863	0.6746	0.1389	0.4961	0.1072	0.3795
0.4786	3.8462	0.4180	2.5000	0.3123	1.6894	0.2332	1.2023	0.1781	0.8941	0.1398	0.6890
0.2369	4.7654	0.3818	3.5146	0.3302	2.5000	0.2628	1.8261	0.2078	1.3788	0.1662	1.0723
		0.2792	4.3548	0.3123	3.3106	0.2728	2.5000	0.2263	1.9239	0.1862	1.5146
		0.1294	4.8728	0.2606	4.0334	0.2628	3.1738	0.2356	2.5000	0.1984	1.9970
				0.1806	4.5901	0.2332	3.7877	0.2263	3.0761	0.2026	2.5000
				0.0813	4.9204	0.1863	4.3253	0.2078	3.6212	0.1984	3.0030
						0.1256	4.7177	0.1781	4.1059	0.1862	3.4854
						0.0557	4.9456	0.1389	4.5039	0.1662	3.9274
								0.0921	4.7940	0.1398	4.3110
								0.0405	4.9605	0.1072	4.6202
										0.0704	4.8432
										0.0308	4.9699

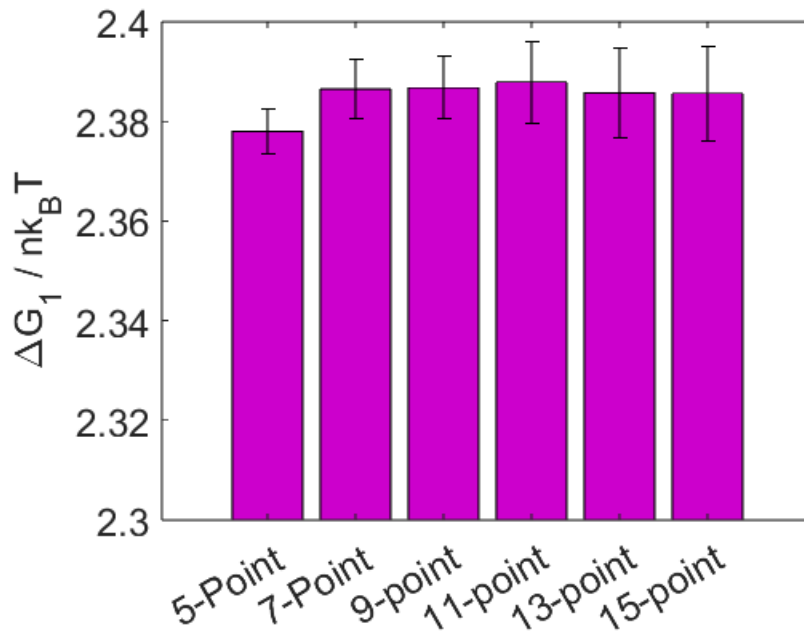


Figure S1: Free energies of Model 1 with varying n -point Gauss-Legendre quadrature.

Enthalpic Contributions in ΔG_1

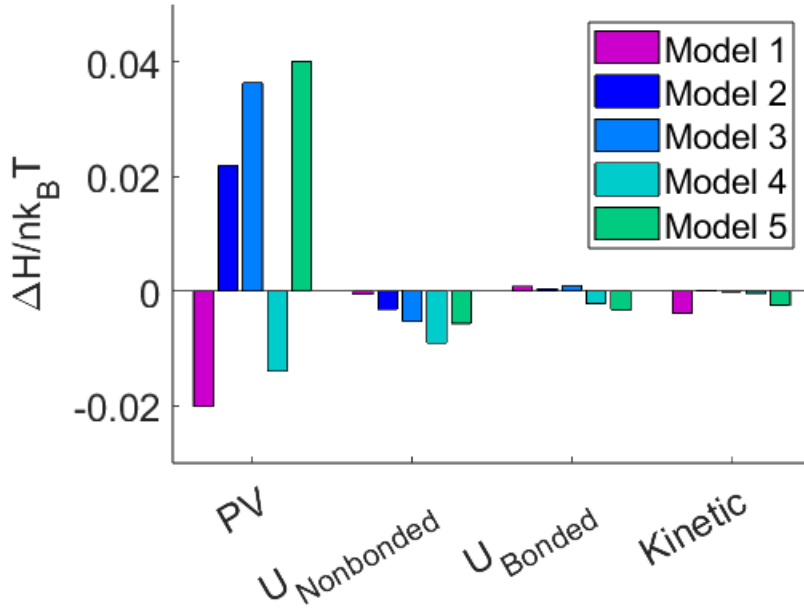


Figure S2: Contributions towards the change in enthalpy caused by the conformational changes associated with increasing the helicity of one block in a BCP melt. Bond angle and dihedral angle contributions are excluded.

Radius of Gyration Tensor

Calculations for the gyration tensor for a relevant group of connected beads provides more detail than simply the radius of gyration. The relevant group could be the entire polymer molecule, or the B -block, comprising N_g beads. The components of the tensor are related to the displacement vector of each bead relative to the center of mass of the group is used to compute the gyration tensor. The position vector of the k^{th} bead is denoted as $(r_x^{(k)}, r_y^{(k)}, r_z^{(k)})$, while that of the center of mass is denoted as $(r_x^{(CM)}, r_y^{(CM)}, r_z^{(CM)})$. The components of the symmetric tensor are defined as:³

$$S_{mn} = \frac{1}{N_g} \sum_{k=1}^{N_g} (r_m^{(k)} - r_m^{(CM)}) (r_n^{(k)} - r_n^{(CM)}); \quad (\text{S2})$$

where m, n cycle through the Cartesian coordinates x, y , and z . The full tensor is symmetric and is given by:

$$S = \begin{pmatrix} S_{xx} & S_{xy} & S_{xz} \\ S_{xy} & S_{yy} & S_{yz} \\ S_{xz} & S_{yz} & S_{zz} \end{pmatrix} \quad (\text{S3})$$

The eigen values of this tensor are designate as L_1, L_2, L_3 where $L_1 < L_2 < L_3$ such that L_1 denotes the largest value. These values are used to calculate the radius of gyration, acylindricity and asphericity. The metrics are related to L_1, L_2 , and L_3 , given by the following formulae.

$$R_g^2 = L_1 + L_2 + L_3 \quad (\text{S4})$$

$$\text{Asphericity } b = L_3 - 0.5 \times (L_1 + L_2) \quad (\text{S5})$$

$$\text{Acylindricity } c = L_2 - L_1 \quad (\text{S6})$$

$$\text{Anistropy } k = \sqrt{\frac{b^2 + \frac{3}{4}c^2}{R_g^4}} \quad (\text{S7})$$

The values of R_g , asphericity b , and acylindricity c are not bounded and will increase as the size of the group increases. The value of anisotropy $k \in [0, 1]$ is bounded. An ensemble average is then applied to the group (each block or entire polymer molecule) and reported in the main text.

Calculation of Kuhn Lengths

The Kuhn lengths for each model at discrete values of K^* required simulations probing single chain polymer statistics. Simulations were initiated for degrees of polymerization (N) ranging from 10 to 500 in a canonical ensemble with simulation box lengths large enough to avoid any interaction through periodic boundaries. A Nose-Hoover thermostat was used to maintain a temperature of $T^* = 1$ with a damping parameter of $100\delta\tau$. The simulations

proceeded with a timestep increment of $\delta\tau = 10^{-3}$ for 3×10^7 timesteps. The contour length of each polymer in these coarse-grained models is dependent on N and the bond length between each bead, l . This is equivalent to the statistical degree of polymerization, M and Kuhn length, b . Therefore by setting $Nl = Mb$ and multiplying both sides by b we get:

$$Mb^2 = R_{ce}^2 = Nlb \quad (\text{S8})$$

Finally, we plot the root-mean-square end-to-end distance against Nl in a model. The slope obtained by fitting a straight line gives the Kuhn length.

Free Energy Calculations For Increasing Chemical Disparity

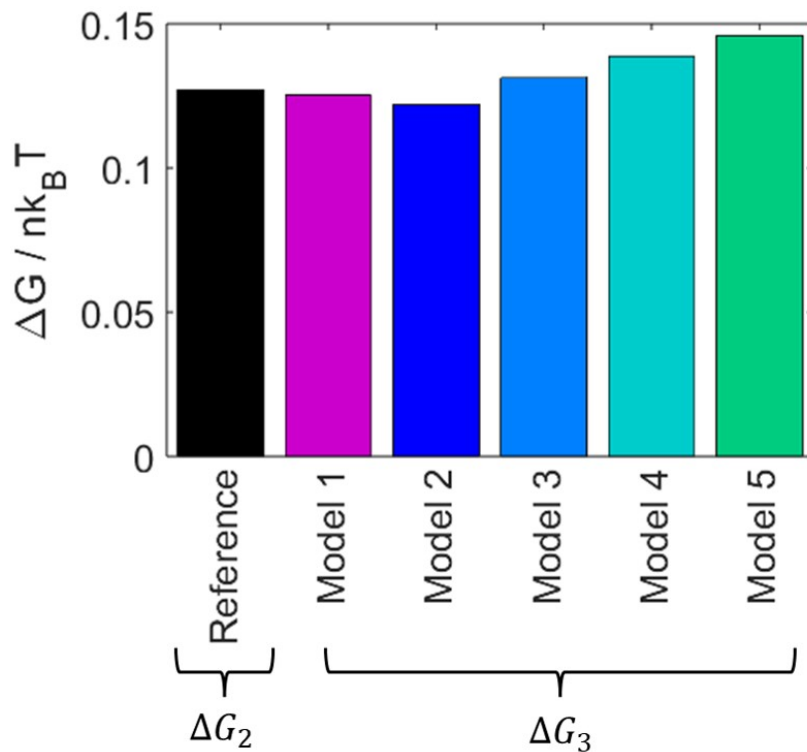


Figure S3: Change in free energy for thermodynamic integration paths 2 and 3.

Structure Factors For Increasing Chemical Disparity

The structure factors $S(q)$ were calculated by:

$$S(q) = \frac{1}{N} \left[\sum_{i=1}^N \cos(\vec{q} \cdot \vec{r}_i) + \sum_{i=1}^N \sin(\vec{q} \cdot \vec{r}_i) \right] \quad (\text{S9})$$

where \vec{r}_i is the position vector for each atom of a system containing N particles and q is the magnitude of the wave vector, \vec{q} incident on the system and takes the form of:

$$\vec{q} = (2\pi n_x/L_x, 2\pi n_y/L_y, 2\pi n_z/L_z) \quad (\text{S10})$$

where n takes on integer values ranging from $[0, L]$. In this study the particles subject to this formulation were the chiral, “B” beads.

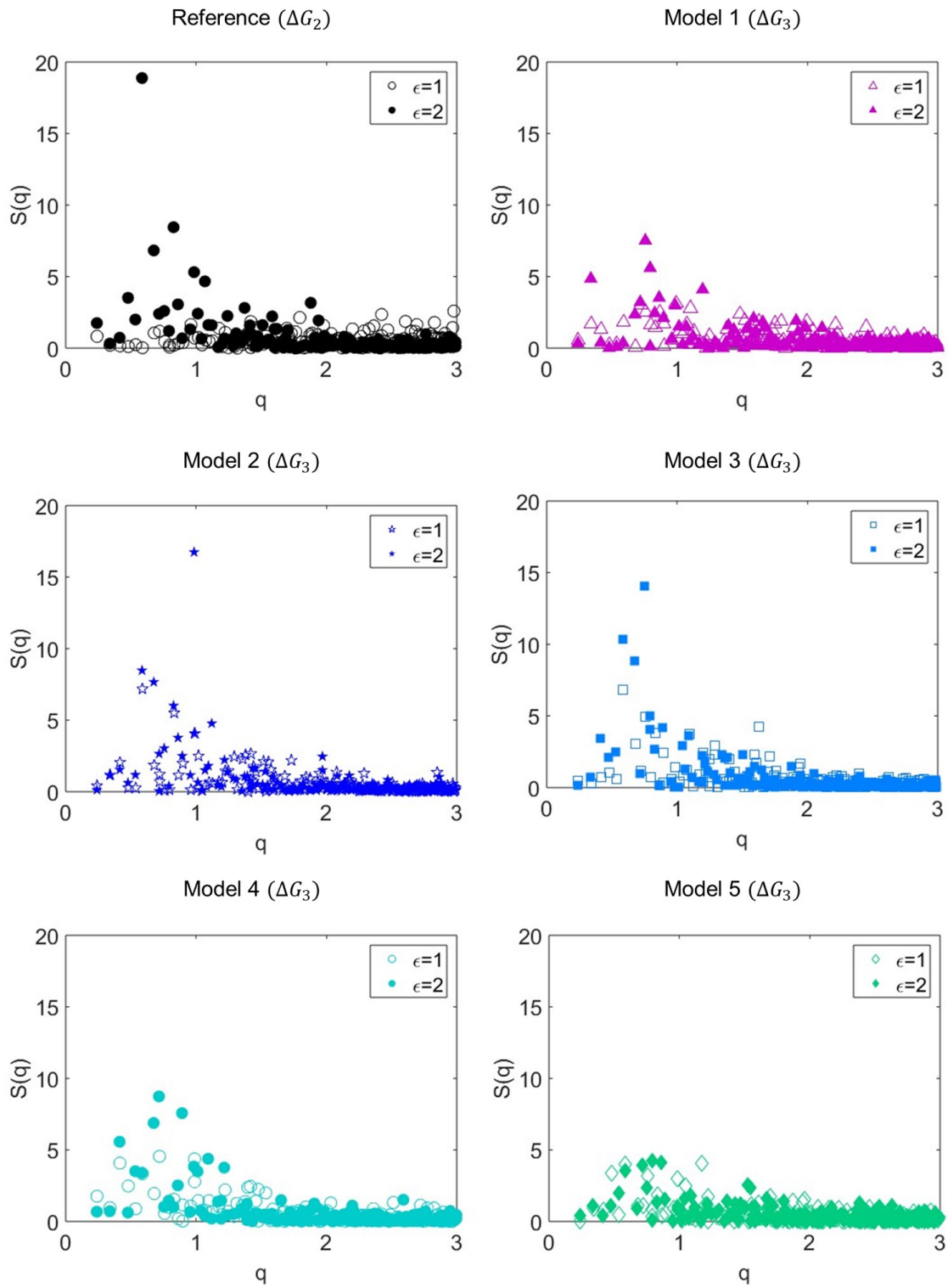


Figure S4: Comparison of structure factors along thermodynamic integration paths 2 and 3.

References

- (1) Seo, Y.; Brown, J. R.; Hall, L. M. Effect of Tapering on Morphology and Interfacial Behavior of Diblock Copolymers from Molecular Dynamics Simulations. *Macromolecules* **2015**, *48*, 4974–4982.
- (2) Humphrey, W.; Dalke, A.; Schulten, K. VMD – Visual Molecular Dynamics, version 1.9.3. *J. Mol. Graphics* **1996**, *14*, 33–38.
- (3) Shape Metrics Formulas. https://isg.nist.gov/deepzoomweb/measurement3Ddata_help, accessed on 09/01/2023.